

On some analytic properties of the atmospheric tomography operator: Non-Uniqueness and reconstructability issues

Ronny Ramlau* Bernadett Stadler†

April 18, 2024

Abstract

In this paper, we consider the atmospheric tomography operator, which describes the effect of turbulent atmospheric layers on incoming planar wavefronts. Given wavefronts from different guide stars, measured at a telescope, the inverse problem consists in the reconstruction of the turbulence above the telescope. We show that the available data is not sufficient to reconstruct the atmosphere uniquely. Additionally, we show that classical regularization methods as Tikhonov regularization or Landweber iteration will always fail to reconstruct a physically meaningful turbulence distribution.

Keywords: Atmospheric tomography operator, ill-posed and ill-conditioned problems

AMS: 78A10, 47A52

1 Introduction

Images from earth bound telescopes are obtained by looking at the sky through the atmosphere. Inhomogenous distributed air patches with different temperature have different refractive indices, which causes the wavefronts of the incoming light from astronomical objects to travel with locally varying speed. This effect reduces the image quality of the obtained astronomical images and worsens for larger telescopes. As a counter-measure, modern giant telescopes are equipped with *Adaptive Optics* systems, which use a combination of wavefront sensors and deformable mirrors for the correction of the incoming disturbed wavefronts [22, 23]. Based on wavefront sensor measurements of distant guide stars, appropriate shapes of deformable mirrors are obtained such that the blurring caused by the turbulence of the atmosphere is removed after reflection, see Figure 1 (left).

Single Conjugate Adaptive Optics (SCAO) is the simplest Adaptive Optics system: The light of a single bright *Natural Guide Star* (NGS) near to the astronomical object of interest is used to compute the optimal correcting shape of a single deformable mirror. The general principle of an SCAO system is given in Figure 1 (right).

More complex AO systems use the incoming light of several guide stars, measured by several wavefront sensors, and multiple deformable mirrors to achieve either a high image quality over a large field of view (*Multi Conjugate Adaptive Optics*, MCAO) or to achieve high image quality in prescribed directions (*Laser Tomography Adaptive Optics*, LTAO, and *Multi Object Adaptive Optics*, MOAO). As there are not enough bright guide stars available at the night sky, artificially created *Laser guide stars*

*Industrial Mathematics Institute, Johannes Kepler University Linz, and Johann Radon Institute for Computational and Applied Mathematics, A-4040 Linz, Austria (ronny.ramlau@jku.at).

†Johann Radon Institute for Computational and Applied Mathematics, A-4040 Linz, Austria (bernadett.stadler@ricam.oeaw.ac.at).

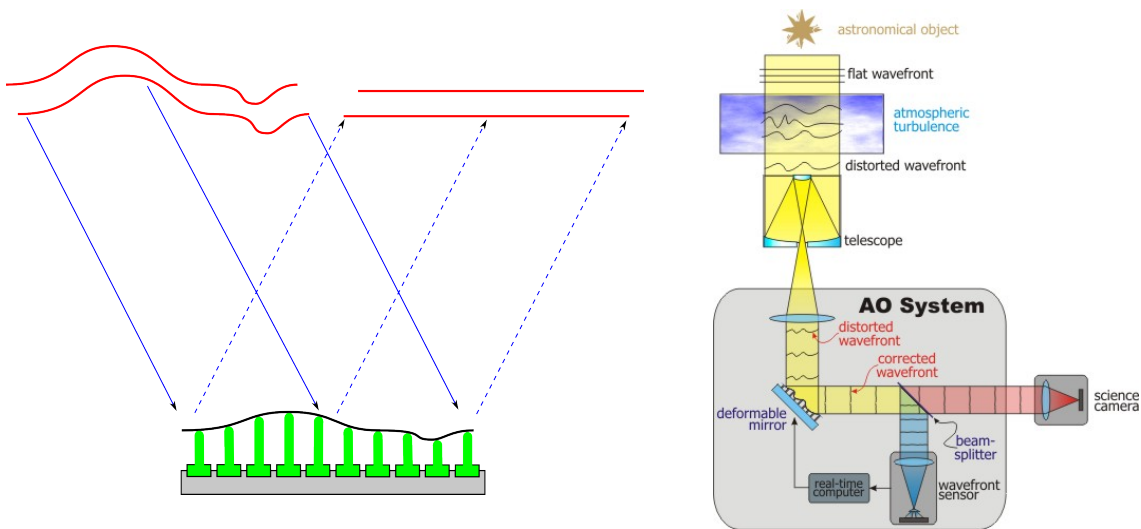


Figure 1: Left: correction of an incoming wavefront by a deformable mirror (image from [1]); Right: sketch of a SCAO system (image from [4]).

(*LGS*) are commonly used. The computation of the mirror shapes for MCAO, LTAO and MOAO is based on the reconstruction of the turbulence profile above the telescope from the incoming wavefront measurements, which is obtained by solving the Atmospheric Tomography problem. As the separation of the guide star is low (1 arcmin for MCAO, 3.5 arcmin for MOAO) we are facing a limited angle tomography problem which is known to be severely ill posed [3, 17]. Moreover, only few data are available, as only a small number of guide stars can be used (e.g., 6 laser guide stars for the *Extremely Large Telescope (ELT)* of the *European Southern Observatory (ESO)*). Thus it is hopeless to attempt to reconstruct the full turbulent volume above the telescope. Instead, we use the common assumption that the atmosphere contains only a limited number of turbulent layers, which are infinitely thin and located at a prescribed height, see Figure 2 for a related MCAO setup.

Atmospheric Tomography has been in the focus of astronomers and AO engineers for years. Its mathematical description can be derived from the standard Radon transform by taking into account the geometry of the telescope, the limited angle property and the layered structure of the atmosphere [6, 9]. Most of the research has been dedicated to the development of numerical reconstruction approaches: e.g., Fusco et.al. [9] propose a minimum mean square error method, while in [10] a back-projection algorithm has been used. In particular popular are conjugate gradient type iterative reconstructors with suitable preconditioning [5, 11, 12, 30, 29]. The Fractal Iterative Method (FrIM) [27, 28, 26] and the Finite Element Wavelet Hybrid Algorithm (FEWHA) [31, 13, 32, 33] both compute maximum a-posterior estimators for the solution of the atmospheric tomography problem, whereas a Kaczmarz iteration is used in [19, 24]. In infinite dimensional function spaces, the atmospheric tomography operator has been considered in [19, 8] with a focus on the derivation of the adjoints of the operator with respect to different underlying function spaces. In a standard L_2 setting, singular value type decompositions [18] as well as frame decompositions [14, 15] have been derived. The singular value type decomposition already suggest the existence of a nonzero nullspace of the atmospheric tomography operator, as some of the "singular values" are numerically zero, but a throughout analysis is still missing. Additionally, the used reconstruction methods all seem to fail to reconstruct the original atmosphere, which is another hint towards a nontrivial nullspace.

The aim of our paper is therefore to gain some insight into the structure of the Atmospheric Tomog-

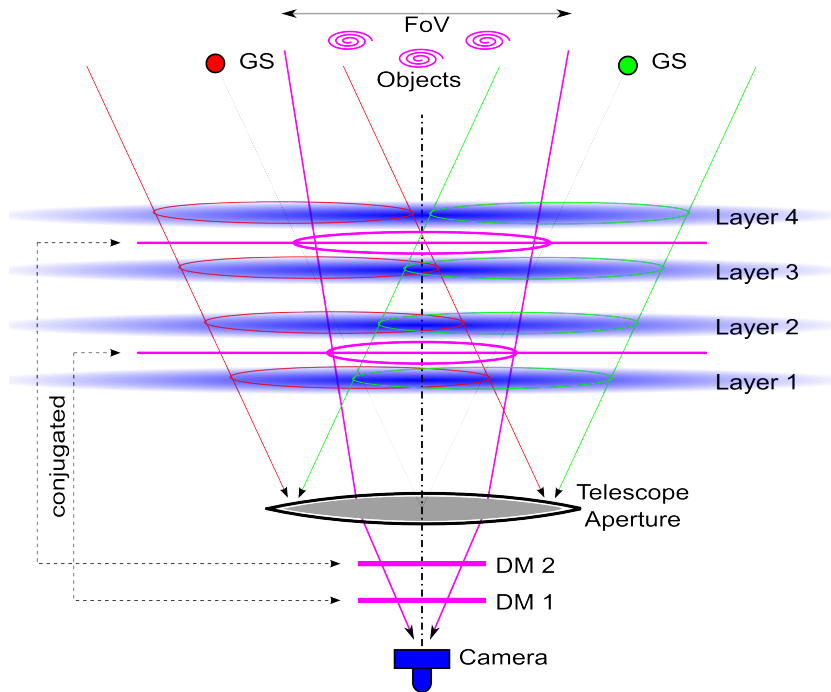


Figure 2: Sketch of an MCAO system assuming a four layer atmosphere and using two deformable mirrors for correction (image from [1]).

raphy problem. In particular, we will show that a proper reconstruction in *non-overlapping* areas is impossible. Additionally, we will investigate the structure of the reconstructions obtained by standard regularization methods which use the adjoint of the atmospheric tomography operator. We will show that those methods almost always fail to fully reconstruct a realistic atmosphere. The analytical results are supported by numerical simulations.

The paper is organized as follows: in Section 2 we define the geometrical setup and define the related atmospheric tomography operator and its adjoint. In Section 3 we show that the atmospheric tomography operator is not uniquely invertible. Section 3.2 analyses the structure of solutions obtained by classical reconstruction methods like Tikhonov regularization, Landweber iteration or the Kaczmarz method. Finally we verify our results numerically in Section 4.

2 Setting

The Atmospheric Tomography operator describes a limited angle tomography problem based on a layered structure of the atmosphere. Additionally, only a finite number of directions of views α_g , $g = 1, \dots, G$, associated to the location of G guide stars (natural or laser) and a wavefront sensor measuring the incoming wavefronts φ_{α_g} from the guide star, are available. We assume that the atmosphere contains L layers, where each layer is a plane at height h_l parallel to the telescope aperture Ω_T (see Figure 3).

A standard setting for the ELT that is also used in our numerical examples is the ESO standard atmosphere with $L = 9$ layers sampled by $G = 6$ viewing directions. This setup is, e.g., used for ELT simulations of the instrument *Multiconjugate adaptive Optics Relay For ELT Observations* (MOR-

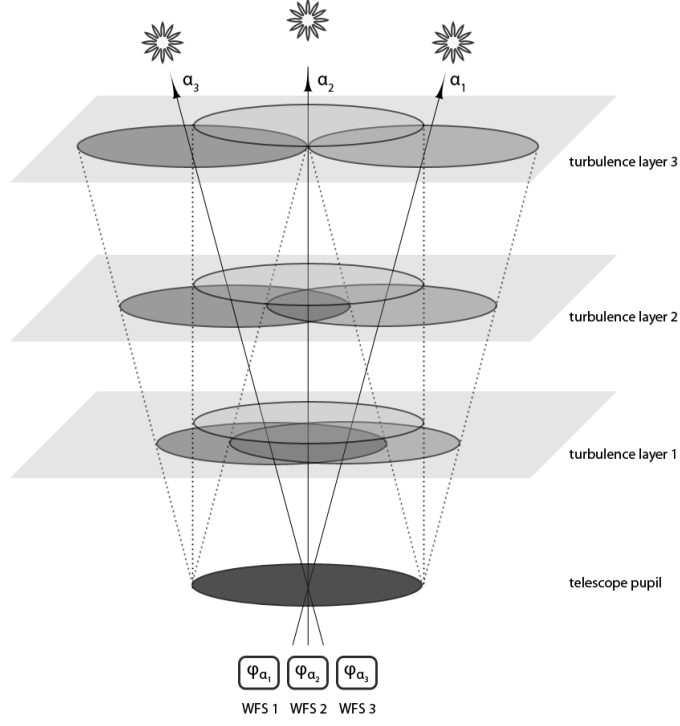


Figure 3: Layered atmosphere with three viewing directions. At each layer, turbulence can only be reconstructed in the intersections of the shifted pupil areas.

FEO). In the following, we will denote the turbulence at layer l by $\Phi^{(l)}$ and the incoming wavefronts in direction α_g by φ_{α_g} . Assuming geometric optics, the connection between the turbulent layers $\Phi = (\Phi^{(1)}, \dots, \Phi^{(L)})^T$ and the incoming wavefronts $\varphi = (\varphi_{\alpha_g})_{g=1, \dots, G}$ is given by the atmospheric tomography operator \mathbf{A} , see [9]:

$$\mathbf{A} : \bigotimes_{l=1}^L L_2(\Omega_l) \rightarrow L_2(\Omega_T)^G \quad (2.1)$$

$$\mathbf{A}\Phi := \varphi = \begin{pmatrix} \varphi_{\alpha_1} \\ \vdots \\ \varphi_{\alpha_G} \end{pmatrix} \quad (2.2)$$

$$\varphi_{\alpha_g}(\mathbf{r}) = \mathbf{A}_{\alpha_g}\Phi := \sum_{l=1}^L \Phi^{(l)}(\mathbf{r} + h_l \alpha_g), \mathbf{r} \in \Omega_T, g = 1, \dots, G. \quad (2.3)$$

The sets Ω_l are defined as

$$\Omega_l = \bigcup_{g=1}^G \Omega_T(h_l \alpha_g), \quad (2.4)$$

$$\Omega_T(h_l \alpha_g) := \{\mathbf{r} \in \mathbb{R}^2 : \mathbf{r} - h_l \alpha_g \in \Omega_T\}. \quad (2.5)$$

The set Ω_l denotes the area on the layer l that contributes to the measurements of φ . This area grows with increasing height, see Figure 3. Please note that this definition only covers the case where the incoming light originates from NGS. For LGS, in particular the cone effect has to be considered, which leads to a slightly different definition of the operator, see, e.g., [24]. Nevertheless, all of the obtained results in the paper can be easily generalized from the NGS to the LGS or mixed case.

For our analysis we further need to specify the underlying function spaces: the cartesian product spaces are equipped with the usual inner products, respectively, i.e.,

$$\langle \phi, \psi \rangle := \sum_{l=1}^L \frac{1}{\gamma_l} \langle \phi_l, \psi_l \rangle_{L_2(\Omega_l)} \quad \langle \varphi, \psi \rangle := \sum_{g=1}^G \langle \varphi_g, \psi_g \rangle_{L_2(\Omega_T)} .$$

The weights γ_l can be used to include the turbulence strength in layer l into the reconstruction. In order to reconstruct the turbulence profile Φ , we need to solve for given $\varphi_{\alpha_1}, \dots, \varphi_{\alpha_g}, \dots, \varphi_{\alpha_G}$ equation (2.2), i.e., the system of equations

$$\mathbf{A}_{\alpha_g} \Phi = \varphi_{\alpha_g}, \quad g = 1, \dots, G. \quad (2.6)$$

Classical reconstruction methods for linear operator equations make frequently use of the adjoint of the operator, which depends on the operator itself as well as on the used inner product. We have the following result:

Proposition 2.1. The adjoint of the atmospheric tomography operator $\mathbf{A} : L_2(\Omega_l)^L \rightarrow L_2(\Omega_T)^G$ is given by

$$\mathbf{A}^* \varphi = \sum_{g=1}^G \mathbf{A}_{\alpha_g}^* \varphi_{\alpha_g} \quad (2.7)$$

with

$$\left(\mathbf{A}_{\alpha_g}^* \varphi_{\alpha_g} \right) (\mathbf{r}) = \begin{pmatrix} \gamma_1 \cdot \varphi_{\alpha_g} (\mathbf{r} - h_1 \alpha_g) \chi_{\Omega_T(h_1 \alpha_g)} (\mathbf{r}) \\ \vdots \\ \gamma_l \cdot \varphi_{\alpha_g} (\mathbf{r} - h_l \alpha_g) \chi_{\Omega_T(h_l \alpha_g)} (\mathbf{r}) \\ \vdots \\ \gamma_L \cdot \varphi_{\alpha_g} (\mathbf{r} - h_L \alpha_g) \chi_{\Omega_T(h_L \alpha_g)} (\mathbf{r}) \end{pmatrix} \quad (2.8)$$

A proof can be found in [19, 25]. Additionally, we have

Proposition 2.1. The operator $\mathbf{A}_{\alpha_g}^*$ is inverted on its range by \mathbf{A}_{α_g} , i.e.,

$$\left(\mathbf{A}_{\alpha_g} \mathbf{A}_{\alpha_g}^* \psi \right) (\mathbf{r}) = \psi(\mathbf{r}), \quad \psi \in L_2(\Omega_T) . \quad (2.9)$$

See [19] for a proof.

3 Non-Uniqueness of the Atmospheric Tomography Operator

In this section we show that the tomography equation (2.2) does usually not admits a unique equation. To achieve this results, we need some geometrical results based on the atmospheric tomography setup.

3.1 Some geometrical considerations

For what follows we need

Assumption 3.1. For the guide star directions $\alpha_g, g = 1, \dots, G$ and the layer heights $h_l, l = 1, \dots, L$ holds

$$\alpha_j \neq \alpha_g \text{ for } j \neq g \quad (3.1)$$

$$0 < h_1 < \dots < h_l < \dots < h_L. \quad (3.2)$$

Specifically, we assume that

$$\alpha_g = (\cos \theta_g, \sin \theta_g) \quad (3.3)$$

with $\theta_g \in [0, 2\pi)$, and $0 \leq \theta_g < \theta_{g+1}$ for $g = 1, \dots, G - 1$, i.e., the directions are ordered clockwise.

Moreover, it will be convenient to define the overlap function ω_l :

Definition 3.1. For a layer $l, l = 1, \dots, L$, we define the overlap function ω_l as

$$\omega_l(\mathbf{r}) := \sum_{g=1}^G \chi_{\Omega_T(h_l \alpha_g)}(\mathbf{r}). \quad (3.4)$$

The overlap function counts to how many of the areas $\Omega_T(h_l \alpha_g)$ a point \mathbf{r} belongs. We immediately observe

Remark 3.1. For the overlap function it holds that

(i) $\omega_l(\mathbf{r}) \in \{0, 1, \dots, G\}$, i.e., it only admits discrete values.

(ii) $\omega_l(\mathbf{r}) = 0 \iff \mathbf{r} \in \left(\bigcup_{g=1}^G \Omega_T(h_l \alpha_g) \right)^\perp$

(iii) $\omega_l(\mathbf{r}) = 1 \iff \exists \tilde{g} \text{ s.t. } \mathbf{r} \in \Omega_T(h_l \alpha_{\tilde{g}}) \setminus \bigcup_{g \neq \tilde{g}} \Omega_T(h_l \alpha_g)$.

(iv) $\omega_l(\mathbf{r}) = G \iff \mathbf{r} \in \bigcap_{g=1}^G \Omega_T(h_l \alpha_g) \neq \emptyset$.

As we can observe from Figure 3, the overlap of the sets $\Omega_T(h_l \alpha_g)$ decreases for higher altitudes h_l . Accordingly, at a certain altitude $h_{disj}(\alpha)$ there is no overlap anymore, i.e., $\omega_l(\mathbf{r}) \in \{0, 1\}$ for all $h_l \geq h_{disj}$.

Proposition 3.1. *Under Assumption 3.1 and $G > 1$ there exists $\mathbf{r}_l \in \Omega(h_l \alpha_g)$ and $\rho_l > 0$ s.t. $\omega_l(\mathbf{r}) = 1$ for all $\mathbf{r} \in B_{\rho_l}(\mathbf{r}_l)$.*

The proof of the above Proposition can be done using standard arguments, e.g., from analytical geometry. For an illustration please see Figure 4. The graphics also gives the idea for the proof: One takes three neighboring areas $\Omega_T(h_l \alpha_g)$, and computes the intersection points of the circles of the two outer areas. Then we draw a line through the center of Ω_T and the intersection point of the two outer circles. The point \mathbf{r}_l is then placed in the middle of the line between the intersection of the two outer circles and the intersection of the line with the middle circle.

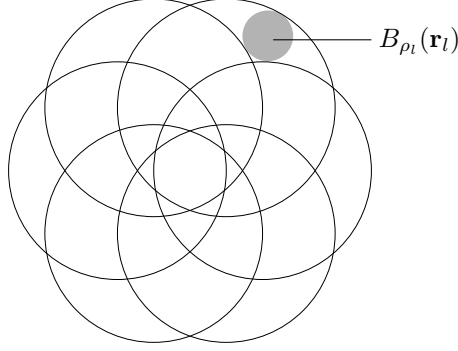


Figure 4: A choice for the ball $B_{\rho_l}(\mathbf{r}_l)$ (dark grey) from Proposition 3.1. For this graphics, 6 different directions α_g have been used.

Proposition 3.2. *Let $\mathbf{r} \in \Omega_T$ and*

$$\tilde{\mathbf{r}} = \mathbf{r} + h_l \alpha_g \quad (3.5)$$

$$\tilde{\tilde{\mathbf{r}}} = \mathbf{r} + h_{l+1} \alpha_g. \quad (3.6)$$

If $\omega_l(\tilde{\mathbf{r}}) = 1$, then also $\omega_{l+1}(\tilde{\tilde{\mathbf{r}}}) = 1$.

Proof. Due to their definition, $\tilde{\mathbf{r}} \in \Omega_T(h_l \alpha_g)$ and $\tilde{\tilde{\mathbf{r}}} \in \Omega_T(h_{l+1} \alpha_g)$. With $\omega_l(\tilde{\mathbf{r}}) = 1$ it holds that $\tilde{\mathbf{r}} \notin \Omega_T(h_l \alpha_{\tilde{g}})$ for all $\tilde{g} \neq g$. As $h_l \alpha_i$ is the center of the circle $\Omega_T(h_l \alpha_i)$, we have in particular

$$\|\tilde{\mathbf{r}} - h_l \alpha_{\tilde{g}}\| > T \text{ for } \tilde{g} \neq g.$$

Showing $\omega_{l+1}(\tilde{\tilde{\mathbf{r}}}) = 1$ is equivalent to proving $\|\tilde{\tilde{\mathbf{r}}} - h_{l+1} \alpha_{\tilde{g}}\| > T$ for all $\tilde{g} \neq g$. For simplicity of notation, we set $h = h_l$, $h_{l+1} = h + \Delta$, $\alpha := \alpha_g$ and $\beta := \alpha_{\tilde{g}}$. We thus obtain

$$\begin{aligned} \|\tilde{\tilde{\mathbf{r}}} - h_{l+1} \alpha_{\tilde{g}}\|^2 &= \|\mathbf{r} + (h + \Delta)\alpha - (h + \Delta)\beta\|^2 \\ &= \|\mathbf{r} + h(\alpha - \beta) + \Delta(\alpha - \beta)\|^2 \\ &= \|\mathbf{r} + h(\alpha - \beta)\|^2 + \Delta^2 \|\alpha - \beta\|^2 + 2\Delta \langle \mathbf{r} + h(\alpha - \beta), \alpha - \beta \rangle \\ &= \|\mathbf{r} + h(\alpha - \beta)\|^2 + (\Delta^2 + 2\Delta h) \|\alpha - \beta\|^2 + 2\Delta \langle \mathbf{r}, \alpha - \beta \rangle. \end{aligned} \quad (3.7)$$

Additionally, we have

$$\|\tilde{\mathbf{r}} - h_l \alpha_{\tilde{g}}\|^2 = \|\mathbf{r} + h(\alpha - \beta)\|^2 = \|\mathbf{r}\|^2 + h^2 \|\alpha - \beta\|^2 + 2h \langle \mathbf{r}, \alpha - \beta \rangle > T^2$$

or

$$\langle \mathbf{r}, \alpha - \beta \rangle > \frac{T^2}{2h} - \frac{h}{2} \|\alpha - \beta\|^2 - \frac{\|\mathbf{r}\|^2}{2h}$$

Using this estimate we obtain with (3.7)

$$\begin{aligned} \|\tilde{\tilde{\mathbf{r}}} - h_{l+1} \alpha_{\tilde{g}}\|^2 &> \|\mathbf{r} + h(\alpha - \beta)\|^2 + (\Delta^2 + 2\Delta h) \|\alpha - \beta\|^2 + \frac{\Delta T^2}{h} - \Delta h \|\alpha - \beta\|^2 - \frac{\Delta \|\mathbf{r}\|^2}{h} \\ &= \|\mathbf{r} + h(\alpha - \beta)\|^2 + (\Delta^2 + \Delta h) \|\alpha - \beta\|^2 + \frac{\Delta T^2}{h} - \frac{\Delta \|\mathbf{r}\|^2}{h}. \end{aligned}$$

Now as $\|\mathbf{r}\| \leq T$ it follows $\frac{\Delta T^2}{h} - \frac{\Delta\|\mathbf{r}\|^2}{h} > 0$, and with $\|\mathbf{r} + h(\alpha - \beta)\| = \|\tilde{\mathbf{r}} - h_l\alpha_{\tilde{g}}\| > T$ it follows

$$\|\tilde{\mathbf{r}} - h_l\alpha_{\tilde{g}}\|^2 > \|\mathbf{r} + h\alpha - h\beta\|^2 + (\Delta^2 + \Delta h)\|\alpha - \beta\|^2 > T^2,$$

which concludes the proof. \square

According to Proposition 3.1, for $h_1 > 0$ it exists

$$\mathbf{r}_1 \in \Omega_T(h_1\alpha_g) \text{ and } \rho_1 > 0$$

such that

$$\mu(B_{\rho_1}(\mathbf{r}_1)) > 0 \quad (3.8)$$

$$B_{\rho_1}(\mathbf{r}_1) \subset \Omega_T(h_1\alpha_g) \quad (3.9)$$

$$\omega_1(\mathbf{r}) = 1 \text{ for all } \mathbf{r} \in \Omega_T(h_1\alpha_g). \quad (3.10)$$

Here, μ denotes the Lebesgue measure. Because of (3.9) there exists for all $\tilde{\mathbf{r}} \in B_{\rho_1}(\mathbf{r}_1)$ an $\mathbf{r} \in \Omega_T$ such that

$$\tilde{\mathbf{r}} = \mathbf{r} + h_1\alpha_g.$$

For what follows, we define

$$\bar{\Omega}_T^g := \{\mathbf{r} \in \Omega_T : \mathbf{r} + h_1\alpha_g \in B_{\rho_1}(\mathbf{r}_1)\} \subset \Omega_T \quad (3.11)$$

$$\bar{\Omega}^{g,l} := \{\mathbf{r} + h_l\alpha_g : \mathbf{r} \in \bar{\Omega}_T^g\} \quad (3.12)$$

and obtain

Proposition 3.3. *With the above definitions we observe*

$$(i) \quad \bar{\Omega}^{g,l} \subset \Omega_T(h_l\alpha_g).$$

$$(ii) \quad \bar{\Omega}^{g,1} = B_{\rho_1}(\mathbf{r}_1).$$

$$(iii) \quad \forall \mathbf{r} \in \bar{\Omega}^{g,l} : \omega_l(\mathbf{r}) = 1.$$

Proof. (i) As $\bar{\Omega}_T^g \subset \Omega_T$, this follows directly from (3.11).

(ii) Follows also directly from the definition of $\bar{\Omega}^{g,l}$ by setting $l = 1$.

(iii) We know that for $\tilde{\mathbf{r}} \in B_{\rho_1}(\mathbf{r}_1) = \bar{\Omega}^{g,1}$ it holds that $\omega_1(\tilde{\mathbf{r}}) = 1$. Additionally, $\tilde{\mathbf{r}} = \mathbf{r} + h_1\alpha_g$ with $\mathbf{r} \in \bar{\Omega}^{g,l}$, therefore

$$\tilde{\mathbf{r}} = \mathbf{r} + h_2\alpha_g \in \bar{\Omega}^{2,g} \quad \forall \mathbf{r} \in \bar{\Omega}_T^g. \quad (3.13)$$

Setting $l = 1$ in Proposition 3.2 yields $\omega_2(\mathbf{r}) = 1$ for all $\mathbf{r} \in \bar{\Omega}^{g,2}$. Now the same argument can be repeated for $l = 2, \dots, L - 1$ and yields $\bar{\Omega}^{g,l+1}$, which finishes the proof. \square

3.2 Non-Uniqueness and Reconstructability

We have now collected all ingredients for a non-uniqueness result for the inversion of the atmospheric tomography operator.

Proposition 3.4. *Under the Assumptions 3.1 with $L > 1$, the atmospheric tomography operator is not uniquely invertible.*

Proof. Let $\Phi = (\Phi^{(1)}, \dots, \Phi^{(L)})$ denote a given atmosphere, and $(\varphi_{\alpha_1}, \dots, \varphi_{\alpha_G})$ the associated wavefronts in the telescope pupil, i.e.,

$$\varphi_{\alpha_g}(\mathbf{r}) = \sum_{l=1}^L \Phi^{(l)}(\mathbf{r} + h_l \alpha_g). \quad (3.14)$$

We want to show that two different atmospheres create the same set of data. It is actually sufficient to show that two atmospheres create the same data φ_{α_g} for a fixed g . According to Proposition 3.1 there exist \mathbf{r}_1 and ρ_1 s.t. $\omega_1(\mathbf{r}) = 1$ for all $\mathbf{r} \in B_{\rho_1}(\mathbf{r}_1)$, and according to Proposition 3.3 (iii) we have $\omega_l(\mathbf{r}) = 1$ for all $\mathbf{r} \in \bar{\Omega}^{g,l}$. Let us restrict our attention to $\mathbf{r} \in \bar{\Omega}_T^g$. Consequently, $\mathbf{r} + h_j \alpha_g \in \bar{\Omega}^{g,l}$, and thus only function values of $\Phi^{(l)}(\mathbf{r})$ in $\bar{\Omega}^{g,l}$ contribute to the function values of $\varphi_{\alpha_g}(\mathbf{r})$ in $\bar{\Omega}_T$. As $\omega_l(\mathbf{r}) = 1$ for all $\mathbf{r} \in \bar{\Omega}^{g,l}$, $\mathbf{r} \notin \Omega_T(h_l \alpha_{\tilde{g}})$ for $g \neq \tilde{g}$ and thus changes in $\Phi^{(l)}$ on $\bar{\Omega}^{g,l}$ leave the computation of $\varphi_{\alpha_{\tilde{g}}}$ unchanged. Next, for $l = 1, \dots, L-1$ we choose

$$\begin{aligned} \tilde{\Phi}^{(l)}(\mathbf{r} + h_l \alpha_g) &= \begin{cases} \Phi^{(l)}(\mathbf{r} + h_l \alpha_g) & \text{for } \mathbf{r} \in \Omega_T \setminus \bar{\Omega}_T^g \\ \text{arbitrarily} & \text{for } \mathbf{r} \in \bar{\Omega}^{g,l} \end{cases} \quad l = 1, \dots, L-1 \\ \tilde{\Phi}^{(L)}(\mathbf{r} + h_L \alpha_g) &= \begin{cases} \Phi^{(L)} & \text{for } \mathbf{r} \in \Omega_T \setminus \bar{\Omega}_T^g \\ \varphi_{\alpha_g}(\mathbf{r}) - \sum_{l=1}^{L-1} \tilde{\Phi}^{(l)}(\mathbf{r} + h_l \alpha_g) & \text{for } \mathbf{r} \in \bar{\Omega}^{g,L}. \end{cases} \end{aligned} \quad (3.15)$$

Consider the related atmospheric tomography data

$$\tilde{\varphi}_{\alpha_{\tilde{g}}}(\mathbf{r}) = \sum_{l=1}^L \tilde{\Phi}^{(l)}(\mathbf{r} + h_l \alpha_{\tilde{g}}).$$

As the atmosphere has only been changed on the sets $\bar{\Omega}^{g,l}$ which are disjunct to $\Omega_T(h_l \alpha_{\tilde{g}})$ for $\tilde{g} \neq g$ we observe $\varphi_{\alpha_{\tilde{g}}} = \tilde{\varphi}_{\alpha_{\tilde{g}}}$. Additionally, we have $\tilde{\varphi}_{\alpha_g}(\mathbf{r}) = \varphi_{\alpha_g}(\mathbf{r})$ for $\mathbf{r} \in \Omega_T \setminus \bar{\Omega}_T^g$ and

$$\begin{aligned} \tilde{\varphi}_{\alpha_g}(\mathbf{r}) &= \sum_{l=1}^L \tilde{\Phi}^{(l)}(\mathbf{r} + h_l \alpha_g) \\ &= \sum_{l=1}^{L-1} \tilde{\Phi}^{(l)}(\mathbf{r} + h_l \alpha_g) + \varphi_{\alpha_g}(\mathbf{r}) - \sum_{l=1}^{L-1} \tilde{\Phi}^{(l)}(\mathbf{r} + h_l \alpha_g) \\ &= \varphi_{\alpha_g}(\mathbf{r}) \quad \mathbf{r} \in \Omega_T \text{ for } \mathbf{r} \in \bar{\Omega}^{g,l}, \end{aligned}$$

i.e., we have shown that $\tilde{\varphi}_{\alpha_{\tilde{g}}} = \varphi_{\alpha_{\tilde{g}}}$ for $\tilde{g} = 1, \dots, G$ although $\Phi^{(l)} \neq \tilde{\Phi}^{(l)}$ for $l = 1, \dots, L$, which concludes the proof. \square

- Remark 3.2.* (i) Please note that changing the atmosphere according to (3.15) may lead to jumps at the boundaries of $\bar{\Omega}^{g,l}$. However, changing the atmosphere smoothly at the boundary of $\bar{\Omega}^{g,l}$ can be done by using the same ideas as above, e.g., by changing the atmosphere as in (3.15), but on an inner subset of $\bar{\Omega}^{g,l}$ and then constructing a smooth transition of the atmosphere from the boundary of the inner subset to the boundary of $\bar{\Omega}^{g,l}$.
- (ii) The construction of two different atmospheres that produce the same data depends on the construction of the set $B_\rho(r_1)$ for a direction α_g with $\omega_1(\mathbf{r}) = 1$ for $\mathbf{r} \in B_\rho(r_1)$. In fact with the same arguments one can show that the atmosphere cannot be uniquely determined in the larger areas where $\omega_l(\mathbf{r}) = 1$ holds.
- (iii) It is easy to see that for systems with large separation, i.e., where the guide stars have a larger distance from each other, the area with no overlap grows. Therefore it will be more difficult to obtain meaningful reconstructions of the atmosphere, which may be an argument against such systems.

In a next step we would like to characterize the solutions that can be reconstructed by standard regularization methods. Let us first review some standard results from regularization theory. For solving a linear equation $Ax = y$, the concept of the generalized solution x^\dagger is frequently used. If $P_{\mathcal{R}(A)}$ denotes the orthogonal projection on $\mathcal{R}(A)$, the range of A , then x^\dagger can be characterized as the (unique) solution of

$$Ax = P_{\mathcal{R}(A)}y$$

with minimal norm, see, e.g., [16, 7]. In particular we have

Proposition 3.5. ([16], Prop. 3.1.1)

The generalized solution $x^\dagger = A^\dagger y$ is the unique solution of the normal equation

$$A^*Ax = A^*y \tag{3.16}$$

in $\overline{\mathcal{R}(A^*)} = \mathcal{N}(A)^\perp$.

Consequently, x^\dagger belongs to $\overline{\mathcal{R}(A^*)}$. Additionally, most of the standard regularization methods produce approximations to x^\dagger that belong to $\mathcal{R}(A^*)$. This is easy to see for Landweber iteration, which is defined by

$$x_{k+1}^\delta = x_k^\delta + \beta A^*(y^\delta - Ax_k^\delta). \tag{3.17}$$

By induction we see that if the initial iterate x_0 belongs to $\mathcal{R}(A^*)$ - which is the case for the standard choice $x_0 = 0$ - then also $x_{k+1} \in \mathcal{R}(A^*)$. The conjugate gradient method has a similar structure, i.e., the update belongs to $\mathcal{R}(A^*)$ and thus also the computed approximation as long as the initial iterate also belongs to $\mathcal{R}(A^*)$. It is also straight forward to see that the minimizer of the Tikhonov functional

$$x_\alpha^\delta = (A^*A + \alpha I)^{-1}A^*y^\delta, \tag{3.18}$$

belongs to $\mathcal{R}(A^*)$. Consequently the structure of $\mathcal{R}(A^*)$ has a significant impact on the reconstructions. As we will see, the existence of the sets $\bar{\Omega}^{g,l}$ results in a specific structure of the adjoint for the atmospheric tomography problem.

Proposition 3.6. For $\varphi = (\varphi_{\alpha_1}, \dots, \varphi_{\alpha_G})$ the adjoint of the atmospheric tomography operator \mathbf{A} on the sets $\bar{\Omega}^{g,l}$ is given by

$$(\mathbf{A}^* \varphi)^{(l)}(\mathbf{r} + h_l \boldsymbol{\alpha}_g) = \gamma_l \varphi_{\alpha_g}(\mathbf{r}) \quad \forall l = 1, \dots, L \text{ and } \mathbf{r} \in \bar{\Omega}_T^g. \quad (3.19)$$

Proof. According to (2.7), (2.8), the adjoint of \mathbf{A} is given as

$$\mathbf{A}^* \varphi = \sum_{g=1}^G \mathbf{A}_{\alpha_g}^* \varphi_{\alpha_g}$$

with

$$\left(\mathbf{A}_{\alpha_g}^* \varphi_{\alpha_g} \right) (\mathbf{r}) = \begin{pmatrix} \gamma_1 \cdot \varphi_{\alpha_g}(\mathbf{r} - h_1 \boldsymbol{\alpha}_g) \chi_{\Omega_T(h_1 \boldsymbol{\alpha}_g)}(\mathbf{r}) \\ \vdots \\ \gamma_l \cdot \varphi_{\alpha_g}(\mathbf{r} - h_l \boldsymbol{\alpha}_g) \chi_{\Omega_T(h_l \boldsymbol{\alpha}_g)}(\mathbf{r}) \\ \vdots \\ \gamma_L \cdot \varphi_{\alpha_g}(\mathbf{r} - h_L \boldsymbol{\alpha}_g) \chi_{\Omega_T(h_L \boldsymbol{\alpha}_g)}(\mathbf{r}) \end{pmatrix}.$$

Now let $\mathbf{r} \in \bar{\Omega}_T^g$. Then $\mathbf{r} + h_l \boldsymbol{\alpha}_g \in \bar{\Omega}^{g,l}$ and

$$\left(\mathbf{A}_{\alpha_g}^* \varphi_{\alpha_g} \right)^{(l)}(\mathbf{r} + h_l \boldsymbol{\alpha}_g) = \gamma_l \varphi_{\alpha_g}(\mathbf{r} + h_l \boldsymbol{\alpha}_g - h_l \boldsymbol{\alpha}_g) \chi_{\Omega_T(h_l \boldsymbol{\alpha}_g)}(\mathbf{r} + h_l \boldsymbol{\alpha}_g) = \gamma_l \varphi_{\alpha_g}(r) \quad (3.20)$$

as $\mathbf{r} + h_l \boldsymbol{\alpha}_g \in \Omega_T(h_l \boldsymbol{\alpha}_g)$ for $\mathbf{r} \in \Omega_T^g$. Moreover,

$$\left(\mathbf{A}_{\alpha_{\tilde{g}}}^* \varphi_{\alpha_{\tilde{g}}} \right)^{(l)}(\mathbf{r} + h_l \boldsymbol{\alpha}_g) = \gamma_l \varphi_{\alpha_{\tilde{g}}}(\mathbf{r} + h_l(\boldsymbol{\alpha}_g - \boldsymbol{\alpha}_{\tilde{g}})) \chi_{\Omega_T(h_l \boldsymbol{\alpha}_{\tilde{g}})}(\mathbf{r}) = 0, \quad (3.21)$$

as $\mathbf{r} + h_l \boldsymbol{\alpha}_g \in \bar{\Omega}^{g,l}$ and $\bar{\Omega}^{g,l} \cap \Omega_T(h_l \boldsymbol{\alpha}_{\tilde{g}}) = \emptyset$ for $g \neq \tilde{g}$. Therefore

$$(\mathbf{A}^* \varphi)^{(l)}(\mathbf{r} + h_l \boldsymbol{\alpha}) = \sum_{\tilde{g}=1}^G \left(\mathbf{A}_{\alpha_{\tilde{g}}}^* \varphi_{\alpha_{\tilde{g}}} \right)^{(l)}(\mathbf{r} + h_l \boldsymbol{\alpha}) = \gamma_l \varphi_{\alpha_g}(r) \quad (3.22)$$

which concludes the proof. \square

Proposition 3.6 has an interesting consequence on the structure of the adjoint on the sets $\bar{\Omega}^{g,l}$:

Proposition 3.7. For $l, k \in 1, \dots, L$ and $\varphi = (\varphi_{\alpha_1}, \dots, \varphi_{\alpha_G})$ holds

$$(\mathbf{A}^* \varphi)^{(l)}(\bar{\Omega}^{g,l}) = \frac{\gamma_l}{\gamma_k} (\mathbf{A}^* \varphi)^{(k)}(\bar{\Omega}^{g,k}). \quad (3.23)$$

Proof. It is

$$\mathbf{r}_l \in \bar{\Omega}^{g,l} \Leftrightarrow \exists \mathbf{r} \in \bar{\Omega}_T^g : \mathbf{r}_l = \mathbf{r} + h_l \boldsymbol{\alpha}_g,$$

and therefore $\mathbf{r}_k = \mathbf{r} + h_k \boldsymbol{\alpha}_g \in \bar{\Omega}^{g,k}$, or more compact,

$$\bar{\Omega}^{g,l} = \bar{\Omega}_T^g + h_l \boldsymbol{\alpha}_g, \quad (3.24)$$

i.e., the sets $\bar{\Omega}^{g,l}$ are shifted versions of $\bar{\Omega}_T^g$. Now, according to (3.19) we obtain for all $\mathbf{r} \in \bar{\Omega}_T^g$

$$\begin{aligned} (\mathbf{A}^* \varphi)^{(l)}(\mathbf{r} + h_l \boldsymbol{\alpha}_g) &= \frac{\gamma_l \gamma_k}{\gamma_k} \varphi_{\alpha_g}(\mathbf{r}) \\ &= \frac{\gamma_l}{\gamma_k} (\mathbf{A}^* \varphi)^{(k)}(\mathbf{r} + h_k \boldsymbol{\alpha}_g) \end{aligned}$$

and therefore (3.23). □

Now according to Proposition 3.5 and the comments thereafter, the generalized solution of the problem

$$\mathbf{A} \Phi = \varphi = (\varphi_{\alpha_1}, \dots, \varphi_{\alpha_G})^T$$

belongs to the range of the adjoint of \mathbf{A} , i.e., $\Phi^\dagger \in \mathcal{R}(\mathbf{A}^*)$, and the same holds for the regularized solutions Φ_{reg}^δ obtained for most of the popular regularization techniques, e.g., for iterative reconstructors or Tikhonov regularization. Thus we derive from Proposition 3.7 the following

Remark 3.3. The generalized solution Φ^\dagger as well as regularized reconstructions that belong to $\mathcal{R}(\mathbf{A}^*)$ have in the sets $\bar{\Omega}^{l,g}$ - apart from a scaling factor - exactly the same values.

Keeping in mind that the original turbulent layers $\Phi^{(l)}$, $l = 1, \dots, L$, are random functions that are independent of each other, it seems unlikely that their function values in the sets $\bar{\Omega}^{l,g}$ differ only by a factor. As a consequence, this would mean that we will only be able to reconstruct turbulences that are not appearing naturally.

3.3 A remark on Landweber-Kaczmarz for Atmospheric Tomography

The structure of the operator \mathbf{A} , i.e., its description by a set of operator equations (2.6) suggests the use of the Landweber - Kaczmarz method, see Algorithm 1.

Algorithm 1 Kaczmarz iteration

```

Choose  $\Phi_0$ 
for  $i = 1, \dots$  do
   $\Phi_{i,0} = \Phi_{i-1}$ 
  for  $g = 1, \dots, G$  do
     $\Phi_{i,g} = \Phi_{i,g-1} + \beta_g \cdot \mathbf{A}_{\alpha_g}^* (\varphi_{\alpha_g} - \mathbf{A}_{\alpha_g} \Phi_{i,g-1})$ 
  end for
   $\Phi_i = \Phi_{i,G}$ 
end for

```

Unfortunately, it has been observed that the method applied to the atmospheric tomography problem does only converge if the scaling parameters β_g are chosen in dependence on the iteration number and decrease towards zero, see [24]. This behaviour may be explained by the following

Proposition 3.8. *Let $\Phi_{k,g-1}$ be arbitrarily given. Then*

$$\Phi_{i,g} = \Phi_{i,g-1} + \beta_g \cdot \mathbf{A}_{\alpha_g}^* (\varphi_{\alpha_g} - \mathbf{A}_{\alpha_g} \Phi_{i,g-1}) \quad (3.25)$$

solves the equation

$$\mathbf{A}_{\alpha_g} \Phi_{k,g} = \beta_g \cdot \varphi_{\alpha_g} + (1 - \beta_g) \mathbf{A}_{\alpha_g} \Phi_{k,g-1}$$

Proof. Applying \mathbf{A}_{α_g} to both sides of (3.25) yields

$$\begin{aligned} \mathbf{A}_{\alpha_g} \Phi_{i,g} &= \mathbf{A}_{\alpha_g} \Phi_{i,g-1} + \beta_g \cdot \mathbf{A}_{\alpha_g} \mathbf{A}_{\alpha_g}^* (\varphi_{\alpha_g} - \mathbf{A}_{\alpha_g} \Phi_{i,g-1}) \\ &\stackrel{(2.9)}{=} \beta_g \varphi_{\alpha_g} + (1 - \beta_g) \mathbf{A}_{\alpha_g} \Phi_{i,g-1}. \end{aligned}$$

□

Remark 3.4. The specific scaling parameter choice $\beta_g = 1$ for all $g = 1, \dots, G$ yields that $\Phi_{i,g}$ solves

$$\mathbf{A}_{\alpha_g} \Phi_{k,g} = \varphi_{\alpha_g}.$$

For the Landweber-Kaczmarz method with scaling parameter $\beta_g = 1$ this means that each new iterate $\Phi_{k,g}$ solves the above equation exactly. If the atmospheric tomography equation $\mathbf{A}\Phi = \varphi$ has a solution Φ^\dagger , and $\mathcal{N}(\mathbf{A}_{\alpha_g}) = \{0\}$ for $g = 1, \dots, G$, then in particular $\mathbf{A}_{\alpha_1} \Phi^\dagger = \varphi_{\alpha_1}$ and the first iterate produces the solution, regardless of the starting value. If, however, solutions of $\mathbf{A}_{\alpha_g} \Phi = \varphi_{\alpha_g}$ do exist that are no solution to (2.2), then it might happen that the iteration jumps in a circular way between those solutions and the iteration does not converge at all with this scaling parameter choice.

4 Numerics

Now let us give some numerical verification to our developed theory. It is a well known issue for MCAO systems that the quality of the AO correction degrades if we move further away from the center. As we will see, we obtain the best correction in the area with highest overlap, i.e., for $\omega_l(x) = G$ for $l=1, \dots, L$ and it drops dramatically with the number of overlaps. For our verification we use a setup similar to the MORFEO instrument [2] of the E-ELT. We simulate three turbulent layers and assume that the deformable mirrors are conjugated to the height of the layers. By doing so, we avoid the fitting step that projects the reconstructed layers onto the deformable mirrors. For the reconstruction process we use different numbers of *Shack Hartmann Wavefront Sensors (SH WFS)*. In this way we vary the amount of data, which impacts the reconstruction quality. The SH WFS consists of a quadratic array of small lenslets and a CCD photon detector lying behind this array. The vertical and horizontal shifts of the focal points determine the average slope of the wavefront over the area of the lens, known as subaperture. For the parameters of the system and the simulation see Table 1 and 2.

Telescope diameter	42m	Layer	Height	Strength
Central obstruction	no	1	0m	0.75
Outer Scale L_0	25m	2	4000m	0.15
Fried parameter	15.7cm	3	12700m	0.1

Table 1: System parameters similar to the MORFEO instrument at the E-ELT and the simulated atmosphere.

As quality criteria for the reconstruction quality we use both the L_2 error of the reconstructed layers and the Strehl ratio. The latter is defined as the ratio between the maximum of the real energy

WFS for NGS		DM	actuators	Height	spacing
#	2-12	1	85x85	0m	0.5m
Type	SH-WFS	2	47x47	4000m	1m
Geometry	84x84 Subap	3	53x53	12700m	1m
# of Photons	10000				
Wavelength	589nm				

Table 2: Simulation parameters of wavefront sensor and deformable mirrors

distribution of incoming light in the image plane $I(x, y)$ over the hypothetical distribution $I_D(x, y)$, which stems from the assumption of diffraction-limited imaging,

$$\text{SR} := \frac{\max_{(x,y)} I(x, y)}{\max_{x,y} I_D(x, y)}. \quad (4.1)$$

By its definition, $\text{SR} \in [0, 1]$; frequently it is also given in %, i.e., $\text{SR} \in [0, 100\%]$. A Strehl ration $\text{SR} = 1$ (100%) means that the influence of the atmosphere has been removed from the observation, i.e., the observation is only diffraction limited. For its numerical evaluation, the Marechal criterion is used. For more details on the Strehl ratio we refer to [22]. The simulations of the forward evaluation have been carried out in the internal and entirely MATLAB-based AO simulation tool MOST, which has been developed by the Austrian Adaptive Optics (AAO) team. The reconstructions have been carried out using the FEWHA algorithm [33, 20, 21]. The evaluation of the Strehl ratios is done at a radially symmetric grid, see Figure 6. Typically, the SH WFS suffers from read-out noise and photon noise. The read-out noise is due to errors while reading photons via the charge-coupled device (CCD) detector planes. This kind of noise is measured in electrons per pixel and set to 3.0 for the simulations. The photon noise is related to the number of photons that are sensed by the CCD in a subaperture during a certain time frame. For an NGS with a large number of photons the noise is commonly approximated by a Gaussian random variable with zero mean and covariance matrix C_η . The noise is identically distributed in each subaperture and the x- and y-measurements are uncorrelated. Hence, the covariance matrix is given by

$$C_\eta = \sigma^2 I, \quad (4.2)$$

where σ^2 is the noise variance of a single measurement defined by $\sigma^2 = 1/n_{\text{photons}}$. In our simulations the number of photons is set to 10000 for all NGS.

Figure 5 shows the original atmosphere on layer 3 as well as its reconstruction based on data from 6 NGS. Visual inspection shows that at least some of the structures in the centre of the atmosphere have been captured, which is not true for structures close to the borders.

In Table 3 we present the reconstruction results, i.e., the L_2 error and the SR, for 6 NGS. The relative L_2 error is calculated via

$$\text{error} := \frac{\|\Phi - \Phi_{\text{rec}}\|_2^2}{\|\Phi_{\text{rec}}\|_2^2}. \quad (4.3)$$

We observe that, although the reconstruction error is decreasing with increasing overlap, it still remains rather large. This is easily explained by the fact that the simulated atmosphere does not necessary belong to the orthogonal complement of the nullspace of the atmospheric tomography operator, whereas our reconstruction belongs to the orthogonal complement, see Remark 3.3. Therefore, the reconstruction error is bounded from below by the norm of its projection to the nullspace,

$$\|\Phi_{\text{rec}} - \Phi^\dagger\| \geq \|\mathcal{P}_{\mathcal{N}(\mathbf{A})}\Phi^\dagger\|.$$

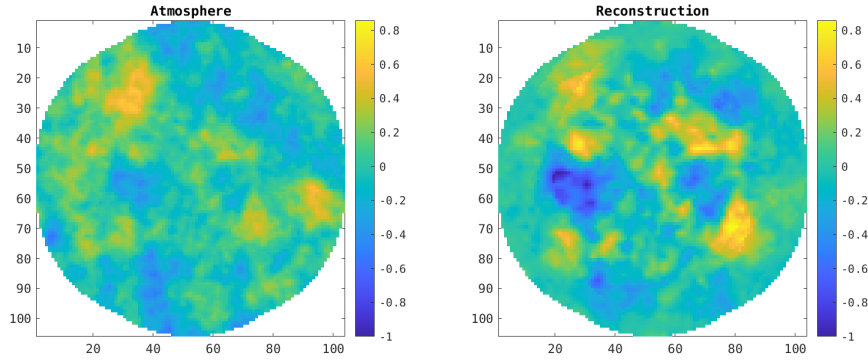


Figure 5: Original turbulence on layer 3 within Ω_3 (left) and its reconstruction using 6 guide stars.

	$\omega_l = 1$	$\omega_l = 2$	$\omega_l = 3$	$\omega_l = 4$	$\omega_l = 5$	$\omega_l = 6$
error	11.72640	1.48710	1.06430	1.01750	0.99180	0.82200
SR	0.00340	0.00640	0.01050	0.02400	0.03720	0.40380
SR variance	0.00070	0.00160	0.00280	0.00670	0.01110	0.17170

Table 3: L_2 error, Strehl Ratio (SR) and SR variance in directions with different numbers of overlaps on Layer 3.

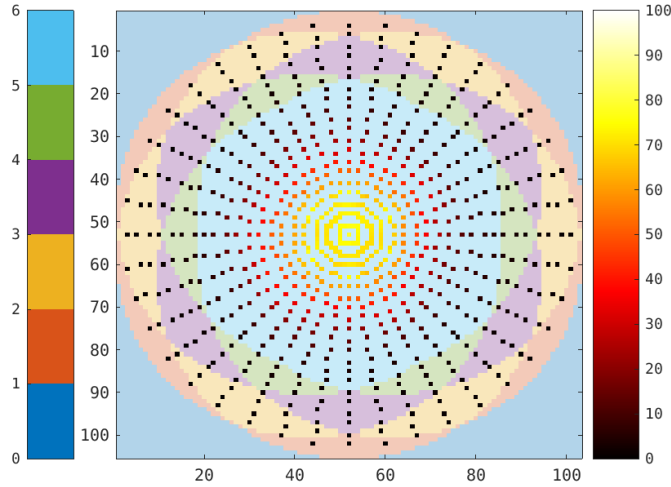


Figure 6: The area Ω_3 on layer 3. The values of $\omega_3(x) \in \{1, \dots, 6\}$ are color coded, see colorbar on the left side of the picture. The dots mark the locations where the Strehl ratio is evaluated. The Strehl ratio achieved at that location are also color coded, see colorbar on the right side of the picture.

Although the reconstruction accuracy is limited, the achievable correction, given by the Strehl ratio, increases significantly and reaches a value of about 0.41 on the third layer with maximal overlap. We

also observe that there is quite a significant jump in the average Strehl Ratio from the area of 5 overlaps to the area of 6 overlaps. This is easily explained by looking at the achieved Strehl ratios within the area of 6 overlaps: while we have in the center Strehl ratios of more than 80%, they drop significantly towards the outer borders of the area, to about 3%, see Figure 6. Additionally, this also can be seen by looking at the variance in Strehl Ratio within areas of same overlaps (last line in Table 3): The variance for the area with $\omega_l = 6$ is by a factor of at least 20 larger than the variances for the other areas. We get similar results with different numbers of guide stars. Note that the average Strehl ratio in the areas with maximal overlaps increases with the number of guide stars, as can be seen in Table 4:

	3 GS	6 GS	9 GS	12 GS
Average SR	0.049	0.3209	0.3418	0.3514
SR Layer 3	0.0624	0.40380	0.4374	0.4529
Center SR	0.1453	0.71210	0.7521	0.7632

Table 4: Strehl ratios in the areas of maximal overlaps for systems with different numbers of guide stars.

In conclusion, we have seen that, although we are unable to reconstruct the correct atmosphere from the given guide star measurements, the achievable *correction* - given by the Strehl Ratio - is high and increases with the number of used guide stars.

Above we have stated that the rather large reconstruction error for the turbulence in Table 3 can be explained by the fact that the simulated atmosphere does not necessarily belong to the orthogonal complement of the nullspace of the atmospheric tomography operator. We now validate this assertion via numerical simulations. To this end, we project the originally simulated atmosphere to the nullspace of the atmospheric tomography operator before reconstructing it. Using $\mathcal{N}(\mathbf{A})^\perp = \mathcal{R}(\mathbf{A}^*)$, we create a projected atmosphere $\hat{\Phi}$ by

$$\hat{\Phi} = \mathbf{A}^* \mathbf{A} \Phi \in \mathcal{N}(\mathbf{A})^\perp. \quad (4.4)$$

Figure 7 shows the projected turbulence and its reconstruction. One easily sees that the difference between the projected $\hat{\Phi}$ here and the original atmosphere Φ in Figure 5 is large and that the projected one does not represent realistic atmospheric conditions. On the other hand, we observe that the reconstruction of the projected atmosphere is now much better than in the original setting in Figure 5. In regions with high overlaps we barely see any differences between the turbulence and its reconstruction, whereas for areas close to the border with a small number of overlaps the reconstruction is less good. This becomes evident when looking at the relative L_2 error in Table 5. In general, the reconstruction error is much smaller compared to the original setting in Table 3. Further, the error is significantly decreasing for areas with a high number of overlaps.

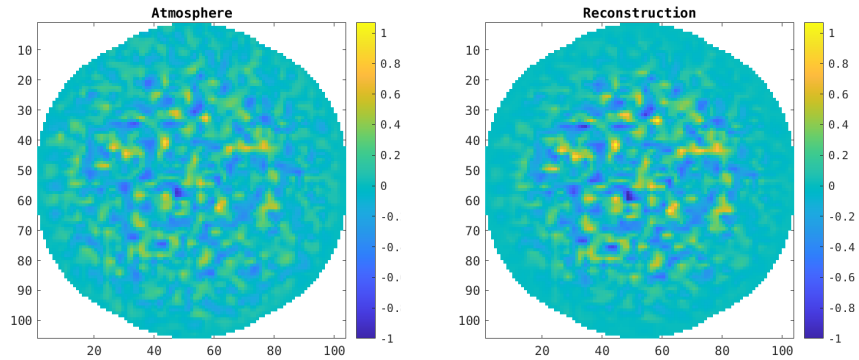


Figure 7: Projected turbulence on layer 3 within Ω_3 (left) and its reconstruction with 6 guide stars.

	$\omega_l = 1$	$\omega_l = 2$	$\omega_l = 3$	$\omega_l = 4$	$\omega_l = 5$	$\omega_l = 6$
error	9.90460	3.17020	1.23490	0.49410	0.30230	0.09400

Table 5: L_2 error for areas with different numbers of overlaps.

5 Conclusion

In the paper we analyzed the Atmospheric Tomography operator in particular with regard to its invertibility. It turns out that especially in non-overlapping areas of the layers there is not enough information in the data in order to achieve a correct reconstruction, which is also confirmed by the numerical simulations. Additionally, the numerical results indicate that in regions with many overlaps a fully correct reconstruction seems impossible. Nevertheless, the AO-correction achieved by the non-optimal reconstruction is still very good in terms of Strehl ratio, which can be explained by the fact that for the correction only the sum of the turbulence along lines is important.

The above results show that the nullspace of the Atmospheric Tomography is rather large, and that standard reconstruction/regularization schemes will almost never succeed in providing an optimal physical reconstruction. If in contrast the atmosphere would belong to the range of the Atmospheric Tomography operator, a reconstruction of the turbulence above the telescope would be possible, as demonstrated by numerical experiments.

The non-uniqueness issues are especially pronounced in the non-overlapping areas. This suggests in particular problems for tomography systems with large angular separation.

References

- [1] G. AUZINGER, *New Reconstruction Approaches in Adaptive Optics for Extremely Large Telescopes*, PhD thesis, Johannes Kepler University Linz, 2017.
- [2] A. BARUFFOLO, I. BARONCHELLI, S. SAVARESE, S. LAMPITELLI, I. FOPPIANI, G. CAPASSO, P. SCHIPANI, A. PETRELLA, D. SELVESTREL, L. BUSONI, G. AGAPITO, C. PLANTET, M. S. VALLES, S. OBERTI, L. PETTAZZI, P. HAGENAUER, R. BIASI, M. MANETTI, D. GRATADOUR, F. RIGAUT, J.-P. VÉRAN, D. KERLEY, M. SMITH, J. DUNN, A. BALESTRA, E. GIRO,

- R. SORDO, S. CHINELLATO, AND P. CILIEGI, *MORFEO at ELT: preliminary design of the real-time computer*, in Adaptive Optics Systems VIII, L. Schreiber, D. Schmidt, and E. Vernet, eds., vol. 12185, International Society for Optics and Photonics, SPIE, 2022, p. 121855K.
- [3] M. DAVISON, *The ill-conditioned nature of the limited angle tomography problem*, SIAM J. Appl. Math., 43 (1983), pp. 428–448.
- [4] V. DHILLON, *Adaptive optics*. http://www.vikdhillon.staff.shef.ac.uk/teaching/phy217/telescopes/phy217_tel_adaptive.html [Accessed: 22-03-16].
- [5] B. ELLERBROEK, L. GILLES, AND C. VOGEL, *Numerical simulations of multiconjugate adaptive optics wavefront reconstruction on giant telescopes*, Applied Optics, 42 (2003), pp. 4811–4818.
- [6] B. ELLERBROEK AND C. VOGEL, *Inverse problems in astronomical adaptive optics*, Inverse Problems, 25 (2009), p. 063001.
- [7] H. ENGL, M. HANKE, AND A. NEUBAUER, *Regularization of Inverse Problems*, Kluwer Academic Publishers, Dordrecht, Boston, London, 2000.
- [8] M. ESLITZBICHLER, C. PECHSTEIN, AND R. RAMLAU, *An $h1$ Kaczmarz reconstructor for atmospheric tomography*, Journal of Inverse and Ill-Posed Problems, 21 (2013), pp. 431–450.
- [9] T. FUSCO, J.-M. CONAN, G. ROUSSET, L. MUGNIER, AND V. MICHAU, *Optimal wave-front reconstruction strategies for multi conjugate adaptive optics*, J. Opt. Soc. Am. A, 18 (2001), pp. 2527–2538.
- [10] D. GAVEL, *Tomography for multiconjugate adaptive optics systems using laser guide stars*, SPIE Astronomical Telescopes and Instrumentation, 5490 (2004), pp. 1356–1373.
- [11] L. GILLES AND B. ELLERBROEK, *Split atmospheric tomography using laser and natural guide stars*, J. Opt. Soc. Am., 25 (2008), pp. 2427–35.
- [12] L. GILLES, C. VOGEL, AND B. ELLERBROEK, *Multigrid preconditioned conjugate-gradient method for large-scale wave-front reconstruction*, J. Opt. Soc. Am. A, 19 (2002), pp. 1817–1822.
- [13] T. HELIN AND M. YUDYTSKIY, *Wavelet methods in multi-conjugate adaptive optics*, Inverse Problems, 29 (2013), p. 085003.
- [14] S. HUBMER AND R. RAMLAU, *A frame decomposition of the atmospheric tomography operator*, Inverse Problems, 36 (2020).
- [15] ———, *Frame decompositions of bounded linear operators in hilbert spaces with applications in tomography*, Inverse Problems, (2021).
- [16] A. K. LOUIS, *Inverse und schlecht gestellte Probleme*, Teubner, Stuttgart, 1989.
- [17] F. NATTERER, *The Mathematics of Computerized Tomography*, Wiley, 1986.
- [18] A. NEUBAUER AND R. RAMLAU, *A singular-value-type decomposition for the atmospheric tomography operator*, SIAM Journal on Applied Mathematics, 77 (2017), pp. 838–853.
- [19] R. RAMLAU AND M. ROSENSTEINER, *An efficient solution to the atmospheric turbulence tomography problem using Kaczmarz iteration*, Inverse Problems, 28 (2012), p. 095004.
- [20] R. RAMLAU AND B. STADLER, *An augmented wavelet reconstructor for atmospheric tomography*, Electronic Transactions on Numerical Analysis (ETNA), 54 (2021), pp. 256–275.

- [21] ———, *Performance of an iterative wavelet reconstructor for the multi-conjugate adaptive optics relay of the extremely large telescope*, *Journal of Astronomical Telescopes, Instruments and Systems*, 8 (2022), p. 021503.
- [22] F. RODDIER, *Adaptive Optics in Astronomy*, Cambridge, U.K. ; New York : Cambridge University Press, Cambridge, 1999.
- [23] M. C. ROGGEMANN AND B. WELSH, *Imaging through turbulence*, CRC Press laser and optical science and technology series, CRC Press, 1996.
- [24] M. ROSENSTEINER AND R. RAMLAU, *The Kaczmarz algorithm for multi-conjugate adaptive optics with laser guide stars*, *J. Opt. Soc. Am. A*, 30 (2013), pp. 1680–1686.
- [25] D. SAXENHUBER AND R. RAMLAU, *A gradient-based method for atmospheric tomography*, *Inverse Problems and Imaging*, 10 (2016), pp. 781–805.
- [26] M. TALLON, C. BÉCHET, I. TALLON-BOSC, M. LE LOUARN, E. THIÉBAUT, R. CLARE, AND E. MARCHETTI, *Performances of MCAO on the E-ELT using the fractal iterative method for fast atmospheric tomography*, *Adaptive Optics for ELTs II*, (2011).
- [27] M. TALLON, I. TALLON-BOSC, C. BÉCHET, F. MOMEY, M. FRADIN, AND E. THIÉBAUT, *Fractal iterative method for fast atmospheric tomography on extremely large telescopes*, in *Proc. SPIE 7736, Adaptive Optics Systems II*, 2010, pp. 77360X–77360X–10.
- [28] E. THIÉBAUT AND M. TALLON, *Fast minimum variance wavefront reconstruction for extremely large telescopes*, *J. Opt. Soc. Am. A*, 27 (2010), pp. 1046–1059.
- [29] C. VOGEL AND Q. YANG, *Fast optimal wavefront reconstruction for multi-conjugate adaptive optics using the Fourier domain preconditioned conjugate gradient algorithm*, *Optics Express*, 14 (2006).
- [30] Q. YANG, C. VOGEL, AND B. ELLERBROEK, *Fourier domain preconditioned conjugate gradient algorithm for atmospheric tomography*, *Applied Optics*, 45 (2006), pp. 5281–5293.
- [31] M. YUDYTSKIY, *Wavelet methods in adaptive optics*, PhD thesis, Johannes Kepler University Linz, 2014.
- [32] M. YUDYTSKIY, T. HELIN, AND R. RAMLAU, *A frequency dependent preconditioned wavelet method for atmospheric tomography*, in *Third AO4ELT Conference - Adaptive Optics for Extremely Large Telescopes*, May 2013.
- [33] ———, *Finite element-wavelet hybrid algorithm for atmospheric tomography*, *J. Opt. Soc. Am. A*, 31 (2014), pp. 550–560.